THE ASTROPHYSICAL JOURNAL, 330:61–77, 1988 July 1

INTERACTING BINARY GALAXIES. IV. SIMULATIONS, MASSES, AND SPATIAL ORIENTATIONS FOR NGC 1587/1588 AND NGC 7236/7237

KIRK D. BORNE[1]
Space Telescope Science Institute[2]
Received 1985 October 3; accepted 1987 December 23

ABSTRACT

We describe here our successful efforts to match interaction models to all of the available data for two pairs of interacting binary galaxies, Nos. 99 and 564 in the Karachentsev catalog of isolated pairs. One of two companion papers (Paper II) describes the physical model and simulation technique, while a second companion paper (Paper III) presents the observational data for these two binaries. That the combined spectroscopic and photometric observations for a binary can be reproduced by an appropriate projection of a particular numerical simulation of the system provides convincing proof of both the gravitational origin of the observed disturbances and of the validity of simple Newtonian gravity on a 10 kpc scale. Exercising very few assumptions, we have been able *to reconstruct the three-dimensional spatial orientation of each pair and thereby to measure its total mass.* Constraints have been placed not only on the masses of the galaxies, but also on their internal dynamical configurations and on the properties of their relative orbit. For the two pairs, K99 and K564, the total masses that we derive are quite reasonable and yield M/L values near 10. Given the success with which these simulations have matched all available data, we conclude that the observed disturbances in rotation velocity and luminosity distribution for these binary galaxies are entirely consistent with the merger hypothesis. Distortions include U-shaped rotation profiles and one-sided luminosity distensions. *These tidal perturbations provide solid observational evidence of tidal friction in action.*

Subject headings: galaxies: individual (NGC 1587/1588, NGC 7236/7237) — galaxies: interactions — galaxies: internal motions

I. INTRODUCTION

Using a simple, physically realistic numerical simulation algorithm as an interpretive tool, we attempt to elucidate in this series of papers the observable properties of colliding galaxies and to identify the effects of these interactions on the subsequent evolution of the participating galaxies. Simulations are presented in this paper for two particular pairs of interacting ellipticals. A complete description of the model is provided in a companion paper (Borne 1988, hereafter Paper II; see also Borne 1984, hereafter Paper I), and the observational data that will constrain the model parameters are presented in a second companion paper (Borne and Hoessel 1988, hereafter Paper III). The motivation for this study is given in detail in the earlier papers. Briefly, the attempt to match numerical simulations to observations of interacting binaries will test (1) the validity of Newtonian gravity on the scale of binary galaxies, (2) the gravitational interaction hypothesis for the origin of the distortions seen in these galaxies, and (3) the merger hypothesis for the evolution of these systems. In order to perform these tests, detailed analyses of specific interacting binary galaxies are needed. When such analyses are performed with the aid of a simple gravitational model, the success or failure of the attempts to match models to data will indicate the validity or invalidity of these various hypotheses. In the end, the attempts do indeed prove successful, thereby rendering a strong validation of those theories (see also Borne, Balcells, and Hoessel 1988; hereafter Paper V).

In Paper II the simulation algorithm and the model-matching procedures are described at length. The case for the uniqueness of the dynamical solutions is covered comprehensively in that paper in general terms and is covered in this paper in very specific and concrete terms. Information pertaining to the particular galaxies under study, including data acquisition and analysis procedures, can be found in Paper III. The observed binaries are K99 (NGC 1587/1588) and K564 (NGC 7236/7237), selected from the catalog of isolated pairs of galaxies compiled by Karachentsev (1972). Paper III contains all of the observational results (both spectroscopic and photometric) that are to be compared with the numerical simulations reported in this paper. Section II presents the details of the best-fit model and of the many failed models for K99; § III does the same for K564. The large collection of failed attempts are included for comparison with the final solutions, for delimiting the range of acceptable solutions, and for indicating the degree to which we can constrain the final solution. Section IV summarizes what we believe we have learned so far and offers some suggestions for further investigations.

II. SIMULATIONS OF K99

Simulations are presented in this section that represent (*a*) the best match to the observations for K99 and (*b*) the large variety of failed attempts to match the data. The results from a coarse scan of the orbital parameter space are presented first in Figures 1 and 2, followed by a detailed look at the effects of varying the internal galaxy parameters in Figures 3, 4, and 6. In addition, the dependence of the simulations on small variations in the orbital parameters is investigated in Figure 5. Tables 1 and 2 present the model parameters that distinguish

[1] Visiting Astronomer, Kitt Peak National Observatory, National Optical Astronomy Observatories, operated by the Association of Universities for Research in Astronomy, Inc., under contract with the National Science Foundation.

[2] Operated by the Association of Universities for Research in Astronomy, Inc., for the National Aeronautics and Space Administration.

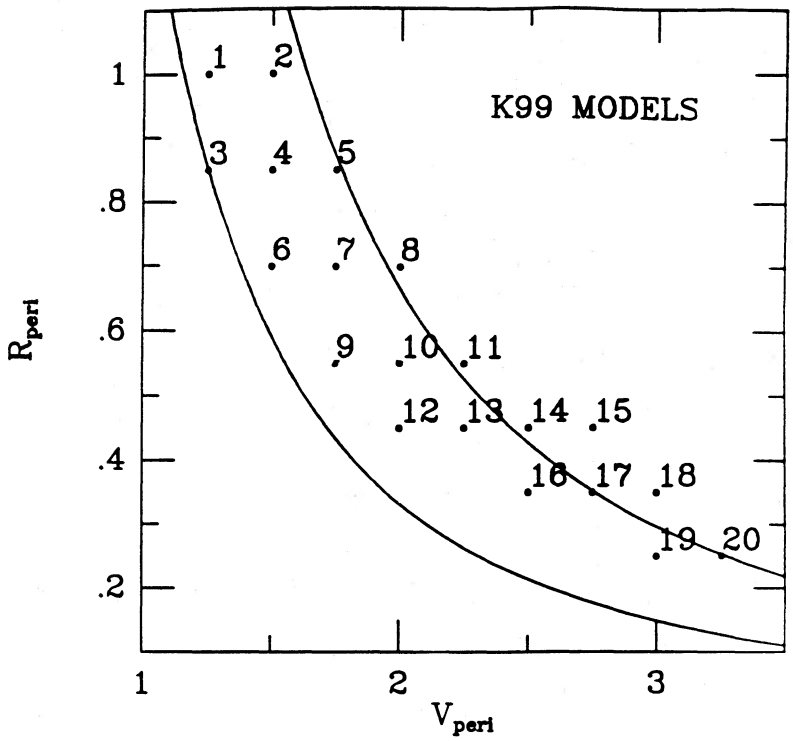

FIG. 1.—Position of orbits in the orbital parameter space for the models listed in Table 1 for K99. Pericenter speed is the abscissa, and pericenter separation is the ordinate. Units are specified in Papers I and II ($G = M_1 = R_1 = 1$). The lower of the two curved lines represents the locus of circular orbits; there are no orbits below this line. The upper curve delineates the position of parabolic orbits; orbits above this line are unbound.

TABLE 1

MODEL PARAMETERS FOR K99 ORBIT SEARCH

MODEL NUMBER	M_2/M_1	R_{peri}	V_{peri}	M_1	M_1 ROTATION		M_2 (no rotation)	REMARKS
					Mode	Axis		
1.....	1/3	1.00	1.25	E0	Refl	(0, 0)	E0	Too slow
2.....	1/3	1.00	1.50	E0	Refl	(0, 0)	E0	Too weak
3.....	1/3	0.85	1.25	E0	Refl	(0, 0)	E0	Too slow
4.....	1/3	0.85	1.50	E0	Refl	(0, 0)	E0	[a]
5.....	1/3	0.85	1.75	E0	Refl	(0, 0)	E0	[a]
6.....	1/3	0.70	1.50	E0	Refl	(0, 0)	E0	Too slow
7.....	1/3	0.70	1.75	E0	Refl	(0, 0)	E0	[a]
8.....	1/3	0.70	2.00	E0	Refl	(0, 0)	E0	[a]
9.....	1/3	0.55	1.75	E0	Refl	(0, 0)	E0	Too strong
10.....	1/3	0.55	2.00	E0	Refl	(0, 0)	E0	[a]
11.....	1/3	0.55	2.25	E0	Refl	(0, 0)	E0	[a]
12.....	1/3	0.45	2.00	E0	Refl	(0, 0)	E0	Too strong
13.....	1/3	0.45	2.25	E0	Refl	(0, 0)	E0	Too strong
14.....	1/3	0.45	2.50	E0	Refl	(0, 0)	E0	Studied in detail
15.....	1/3	0.45	2.75	E0	Refl	(0, 0)	E0	Too fast
16.....	1/3	0.35	2.50	E0	Refl	(0, 0)	E0	Too strong
17.....	1/3	0.35	2.75	E0	Refl	(0, 0)	E0	[a]
18.....	1/3	0.35	3.00	E0	Refl	(0, 0)	E0	Too fast
19.....	1/3	0.25	3.00	E0	Refl	(0, 0)	E0	Too fast
20.....	1/3	0.25	3.25	E0	Refl	(0, 0)	E0	Too fast

[a] Several models provided evidence in their surface density maps for a good match to K99. However, it was not possible to simultaneously match all of the data: isophotal distortions, galaxy flattening, relative velocity, and rotation profiles.

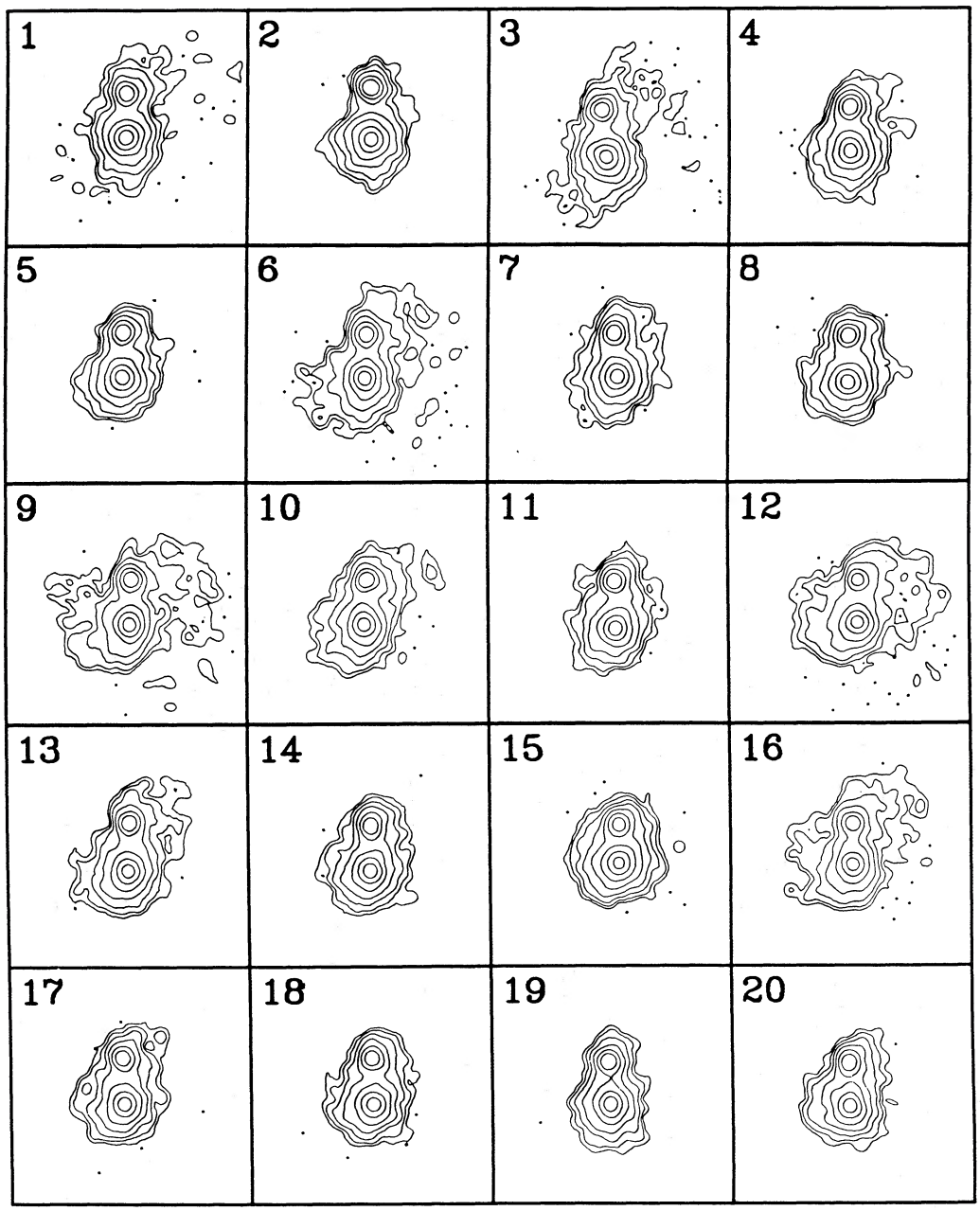

FIG. 2.—Top views of the attempted models for K99, where each box is numbered according to the key in Table 1 (and Fig. 1). Surface density contour levels are spaced at 1.0 mag intervals. Each model is shown at the time when the separation of the pair and the degree of distortion are as close to the real data as the simulation allows. Note the strong variations in the distortions as a function of the orbital parameters.

the various simulations that are portrayed in this series of surface density contour diagrams. Figures 7 and 12, with Table 5, present the adopted physical solution for K99: rotation and dispersion velocity profiles, a surface density contour "image," and a tabulation of the orbit properties (e.g., orbit inclination, orbital phase, line of nodes, and masses).

a) K99 Mass Ratio

The ratio of the velocity dispersion for the smaller component of K99 (hereafter K99-2) to that for the primary component (hereafter K99-1) is 0.67 (Paper III). If their mass-to-light ratios are nearly equal and if the $L_V \propto \sigma^4$ relationship is assumed valid here (Faber and Jackson 1976; Sargent *et al.* 1977; Terlevich *et al.* 1981), then the mass ratio for the K99 binary would be $M_2/M_1 \approx 1/5$. If equation (11) of Paper II holds true, we expect that $R_2/R_1 \approx 0.45$, which is found to be an accurate representation of at least the intermediate isophotal radii for the two galaxies in Figure 2 of Paper III, thus providing some justification for using 1/5 as the K99 binary mass ratio. However, a quantitative study of the CCD images indicates that the luminosity ratio is more like 1/3, calculated both from the total light of each galaxy and from the light inside the smallest common isophote. If the mass-to-light ratios are again assumed to be nearly equal in the two galaxies, we would now guess the mass ratio to be 1/3. Since we do not know *a priori* the contribution of dark matter to each galaxy

TABLE 2

PARAMETERS FOR MODELS NEAR THE BEST ORBIT FOR K99

MODEL	R_{peri}	V_{peri}	M_1	ROTATION Mode	ROTATION Axis	M_2	MINOR AXIS (no rotation)	AREAS OF MISMATCH IN SURFACE DENSITY MAPS
A	0.45	2.60	E3	Refl	(15, 10)	E4	(90, 170)	P.A. of M_1 flattening
B	0.45	2.60	E3	Refl	(45, 10)	E4	(90, 170)	None
C	0.45	2.60	E3	Refl	(60, 10)	E4	(90, 170)	Roundness of M_1
D	0.45	2.60	E3	Refl	(45, 40)	E4	(90, 170)	Roundness of M_1
E	0.45	2.60	E3	Refl	(45, −20)	E4	(90, 170)	Weak distortion in M_1
F	0.45	2.60	E3	Refl	(45, 10)	E4	(90, 200)	P.A. of M_2 distortion
G	0.45	2.60	E3	Refl	(45, 10)	E4	(90, 140)	P.A. of M_2 distortion
H	0.45	2.60	E3	Refl	(45, 10)	E4	(120, 170)	P.A. of M_2 distortion
I	0.45	2.60	E3	Refl	(45, 10)	E4	(60, 170)	P.A. of M_2 distortion
J	0.45	2.55	E3	Refl	(45, 10)	E4	(90, 170)	None
K	0.40	2.60	E3	Refl	(45, 10)	E4	(90, 170)	Shape of M_2 distortion
L	0.50	2.60	E3	Refl	(45, 10)	E4	(90, 170)	Shape of M_2 distortion
M.....	0.45	2.45	E3	Refl	(45, 10)	E4	(90, 170)	Lack of tail on M_2
N	0.45	2.70	E3	Refl	(45, 10)	E4	(90, 170)	Double tail on M_2
O	0.45	2.50	E3	Refl	(45, 10)	E4	(90, 170)	Weak tail on M_2
P	0.45	2.65	E3	Refl	(45, 10)	E4	(90, 170)	Slight double tail on M_2
Q	0.45	2.60	E0	Refl	(0, 0)	E0	...	Very weak distortions

and since we cannot guarantee the validity of the Faber-Jackson relation for individual galaxies, we must somehow choose between the two values just estimated for the mass ratio, or maybe choose a third unknown value. A preliminary study (not reported here) of many detailed simulations for K99 using the two mass ratios 1/5 and 1/3 indicated that the ratio 1/3 is most likely correct. Essentially what happened was this: in the simulations with the 1/5 mass ratio, the distortions in the primary component of the pair (representing K99-1) were insignificant, if not altogether absent. In those models, the mass of the smaller galaxy was not sufficient to inflict as much tidal damage on its more massive neighbor as we actually see in the CCD image for K99-1 (Paper III). The 1:3 mass ratio was therefore adopted for all of the simulations of K99 listed in this paper; the final adopted solution fits so well to the observational data that it was deemed unnecessary to investigate other possible values for the mass ratio. For the models shown in Figure 2, the number of test particles comprising each galaxy were $N_1 = 1500$ and $N_2 = 500$ for galaxy 1 and galaxy 2, respectively. In all of the remaining figures that present simulations of K99, beginning with Figure 3, $N_1 = 3000$ and $N_2 = 1000$.

b) *Internal Galaxy Properties*

From the rotation observed in K99-1 (see Fig. 4 of Paper III), it was clear that no model would be complete without a similar amount of internal rotation. Since no rotation was evident in K99-2, other than the nonsteady U-shaped rotation (see Paper III), it was not found necessary to add any rotation to its models. Hence, for the simulations reported in this paper, only M_1 (representing K99-1) was given some rotation. In all cases, the rotation of galaxy 1 was generated with 100% particle participation in the reflection algorithm (§ V of Paper II). For the models shown in Figure 2, the rotation axis was pointing at the observer (i.e., parallel to the binary rotation axis). Models shown in subsequent figures have the M_1 rotation axis tited at an oblique angle relative to the observer and the orbital rotation axis; this was required to enforce a match between the model and the observed rotation rate. Small corrections to the tilt of the rotation axis may slightly improve the existing fit (Fig. 7), although the rotation model itself is the biggest cause for concern (see § II*e*).

Both K99-1 and K99-2 show a measurable ellipticity in Figure 2 of Paper III. Hence, flattening is also required in our models. Since the models shown in Figure 2 (to be described below) were run mainly to test the effects of orbital variations on the appearance of distortions in the model galaxies, no flattening was imposed on those models. Subsequent figures portray models in which each galaxy has nonzero flattening (compare Tables 1 and 2). The degree of intrinsic flattening applied to each model galaxy (according to the formula given in eq. [16] of Paper II) was ultimately fixed on a certain reasonable value in order to focus more attention on the parameters that were found to most significantly affect the final match between model and data. Those parameters, whose discussion will now be presented, were (i) the orbit parameters, pericenter speed (V_{peri}) and pericenter separation (R_{peri}), and (ii) the directions of the M_1 rotation/minor axis and of the M_2 minor axis (where M_2 represents K99-2).

c) *Possible Orbits for K99*

Paper II discussed at length the use of the $R_{peri} - V_{peri}$ diagram in isolating a unique orbital solution for a pair of interacting galaxies. That same device is used in this paper to investigate the properties of possible models for the specific pairs studied here. Figure 1 presents such a diagram for the mass ratio 1/3 in our model units: $G = M_1 = R_1 = 1$, where M_1 is the mass of the primary galaxy and R_1 is its tidal radius (see Paper I).

In Figure 1, two curved lines are drawn: the lower curve represents the locus of circular orbits and the upper indicates the location of parabolic orbits. No orbits are allowed below the lower curve, while those above the upper curve are on unbound trajectories. Strongly unbound trajectories can be eliminated for two reasons: (1) the observed relative velocity is too small (even though, of course, the projection is not yet known; see Table 5 for that), and (2) the photometric distortions would be much smaller than we actually observe for two galaxies as close as the K99 pair. Paper II described in detail how the distortions in fast (i.e., strongly unbound) passages are

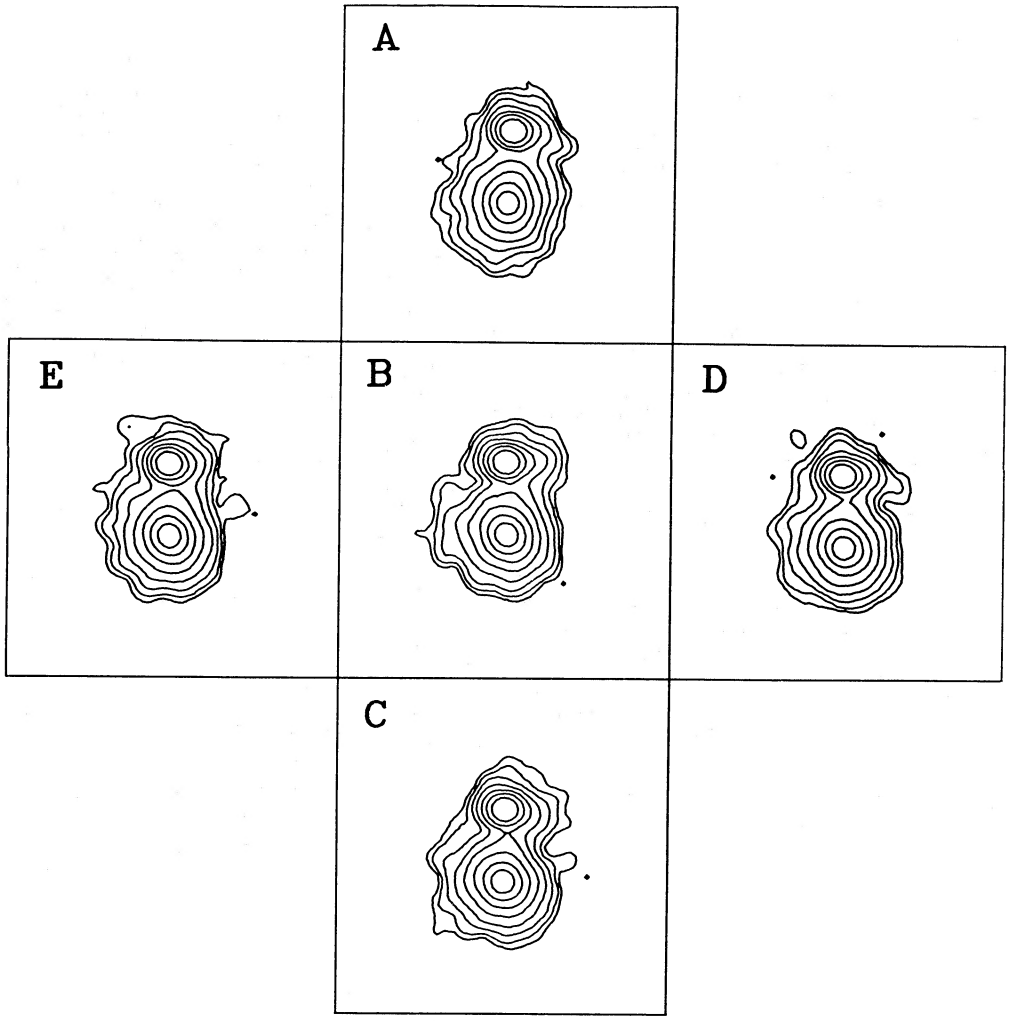

FIG. 3.—Surface density contours of flattened K99 models near the best-fit orbit. Each model is shown at a time and from a viewing angle that allow the best match to both the velocity and photometric data. Each box is labeled according to the key in Table 2. Box B shows the best-fit model for K99. Boxes A and C show models for which the M_1 rotation axis is tilted 30° closer to and farther from orbital rotation axis than in model B, respectively. Boxes D and E show models for which the M_1 rotation axis is precessed $\pm 30°$ from model B relative to the true position angle (i.e., orbital phase) of galaxy 2. Note the slight, although significant, dependence of the apparent ellipticity and observed distortions in galaxy 1 on the M_1 rotation axis (= minor axis).

usually weak and, even so, do not appear until the galaxies are widely separated. We investigated some strongly unbound orbits for K99 and found that the discussion of Paper II proved true for this specific system.

We present here the results of a study of 20 possible orbits for K99, some of which are on bound elliptical trajectories and some of which are slightly unbound. All bound-orbit simulations began at apocenter, and all unbound binary models were started at a time that preceded pericenter passage by ~8–10 crossing times. The 20 orbits that were studied are marked in Figure 1 and are labeled in accordance with the model numbers given in Table 1. Figure 2 uses these same model numbers to display the best possible matches between the imaging data for K99 and the model binary galaxies that were evolved along these orbits.

Table 1 tabulates the initial parameter values for the 20 possible orbits of K99 that were marked in Figure 1. In all of these orbits, the following inputs were constant: the mass ratio ($M_2/M_1 = 1/3$), the number of test particles ($N_1 = 1500$ and $N_2 = 500$), the lack of flattening in M_1 and M_2 (both E0), and the rotation properties of M_1. As stated above, M_1 had 100% particle partcipation in the reflection mode of rotation (§ Vc of Paper II), with the axis of rotation parallel to the orbital angular momentum axis. Throughout this paper the angles that locate the rotation axes of our model galaxies are those of a spherical polar coordinate system: (θ, ϕ), where θ is the polar angle and is measured from the binary orbital angular momentum axis (also the z-coordinate axis), and ϕ is the azimuthal angle and is measured dynamically from the nonstationary line in the orbital plane connecting M_1 and M_2. Spherical polar coordinate angles specified by (0, 0), as in Table 1, refer to the direction parallel to the z-coordinate axis.

The models listed in Table 1 differ only in their initial orbits, as defined by $R_{\rm peri}$ and $V_{\rm peri}$. Since pericenter passage time Δt varies like $R_{\rm peri}/V_{\rm peri}$, the lower numbered orbits have slow (long-duration) encounters, while the higher-numbered orbits have fast (short-duration) pericenter passages. It is also possible to estimate the tidal impulse from these two orbit parameters (see § IX and Fig. 4 of Paper II): $W_{\rm tidal} \sim (R_{\rm peri}\, V_{\rm peri})^{-1}$. As expected, the most strongly bound orbits result in the largest

tidal impulse. Table 1 includes remarks on the outcome of the various simulations: some encounters are too weak, some too fast, and so on. Figure 2 presents surface density contour diagrams for these binaries, numbered according to the key in Table 1 (and Fig. 1). The time of observation for each of these models was chosen to be that which offered the best possible match to the observed distortions in K99. The degree of distortion correlates with the remarks recorded in Table 1.

Several orbits in Table 1 led to a pair of galaxies that looked similar to Figure 2 of Paper III. These orbits (i.e., Nos, 4, 5, 7, 8, 10, 11, 14, and 17) follow roughly a line of constant tidal impulse. Each of the orbits along that line was studied in great detail with realistic rotation axes for K99-1 (i.e., not parallel to the orbital angular momentum axis) and with realistic flattenings in the two galaxies. Only one of those orbits proved successful in matching all the observational data. The others were rejected due to their failure to match either (1) the detailed rotation velocity profiles of K99-1 and K99-2, (2) the ratio of projected relative velocity to the central velocity dispersion in K99-1, or (3) the observed shapes of the two galaxies, including flattening, tidal distortion, and the tidal tail on K99-2. In lieu of showing all of those many poor models, a manageable set will be presented in the next section. Those that will be presented are all in the neighborhood of model 14 of Table 1. They will demonstrate the extent to which the many input parameters can vary before a successful match to the observations is lost. Using input parameters outside of the depicted range (i.e., moving up to models 4, 5, 7, 8, 10, or 11, or moving down to model 17) rendered much poorer fits to the data than will be shown below. These rejected models, which Figure 2 led us to believe were quite reasonable fits, demonstrate in practice what was argued very strongly in words in Papers II and III: that the addition of velocity data (even minimal kinematic measurements) are essential to the identification of a unique model for a particular pair of interacting galaxies.

d) Isolating a Unique Model for K99

A series of simulations around the best-fit model for K99 are presented in this section to demonstrate the degree to which a unique solution can be isolated. That the solution is unique was argued in the previous section on the basis that only this one model was able to fit both the imaging and kinematic data available for K99. That the uniqueness arguments of that section are true will be made manifest in this section as we see that the apparent fit to the data deteriorates when the models move from the preferred point in parameter space.

Table 2 tabulates the range of model parameters used to isolate the unique solution for K99. Seventeen models are listed, each assigned a letter designation corresponding to a surface density map in Figures 3, 4, 5, or 6. Only models J, O, and P are not displayed anywhere. Model J is very similar to our accepted model B and may be considered equal to that one. Models O and P are weak versions of models M and N, respectively; they simply do not show the deterioriation of the fit as clearly as models M and N do. Among the 17 models, the following inputs were constant: the mass ratio ($M_2/M_1 = 1/3$), the number of test particles ($N_1 = 3000$ and $N_2 = 1000$), the ellipticity (i.e., flattening) of M_1 (E3), the ellipticity of M_2 (E4), and the rotation mode of M_1 (100% particle participation in the reflection mode). Between the 17 models, the differences were: the orbit parameters (R_{peri} and V_{peri}), the direction of the M_1 rotation/minor axis, and the direction of the M_2 minor axis. Brief remarks are recorded in Table 2 indicating why a particular model failed to match the imaging data for K99. All of the models depicted in the following figures are shown at the time when its appearance most nearly matched the observations of K99.

Figure 3 shows the effects of varying the direction of the M_1 rotation/minor axis. The best-fit model B is shown in the center of the figure, as well as in the center of Figures 4 and 5. The observer is 40° above the orbital plane (i.e., 50° from the pole), at an azimuth 100° ahead of M_2 in its counterclockwise orbit. The good match between Figure 2 of Paper III and model B is evident for galaxy 1 in (1) the ellipticity at small radii, (2) the position angle of flattening at small radii, and (3) the photometric distortion (i.e., asymmetry) at large radii. At least one of these three match points fails in models A, C, D, and E. A few models with a rotation axis for galaxy 1 tilted more than 30° away from that of model B were examined: they all failed miserably on all three points.

Figure 4 shows the effects of varying the direction of the M_2 minor axis. The good match between Figure 2 of Paper III and model B is evident for galaxy 2 in (1) the ellipticity at small radii, (2) the position angle of flattening at small radii, (3) the existence of a photometric tail extending to the right of the galaxy, and (4) the position angle of the tail. Each of the other models (F, G, H, and I) presents a flattened galaxy 2 at the wrong position angle.

Figure 5 show the effects of small variations in the orbit parameters, smaller than those of Table 1 (as depicted in Figs. 1 and 2). The most serious discrepancy arises in the development of the tail (or tails) on galaxy 2. This tail is in fact the feature of K99 that is most sensitive to the various input parameters and, accordingly, has been used to reject the majority of the failed orbits. Here models K and N (and maybe even model L) show evidence for an additional countertail in addition to the expected orthogonal tail, while model M shows no evidence for a tail at all. Model L shows almost as much distension on the left side of galaxy 2 as on the right side (where the tail is located).

Figure 6 presents the best-fit model B again, both from the derived best viewing angle and from down the orbital rotation axis. As stated above, the observer at the oblique viewing angle is 40° above the orbital plane at a position angle 100° ahead of galaxy 2. For comparison, a simulation (model Q) was run using the same orbital parameters as model B, but with internal galaxy parameters like those of Table 1. The viewing angles of model Q in the two frames are the same as those of the model B view to its immediate left. Note the weakness of the distortions in model Q and the clear indication of the importance of including flattening in such models.

e) The Adopted K99 Solution

Model B of Table 2 provides the input model parameters for the simulation that best matches all of the observational data for K99. In Table 5 a complete array of physical properties and projection angles for K99 are tabulated. Table 5 quotes the value for the absolute B magnitude that was obtained from a study of a larger sample of interacting binaries; the complete set of absolute photometric measurements obtained in that investigation will be described in a later paper. Apart from the B magnitude, all other parameters listed in Table 5 are derivable from information provided in this paper or in Paper III, except for the virial estimate of the mass of K99-1. For that estimate, a value of the effective radius equal to 0.25 was assumed. Most noteworthy in this table is the precision (and

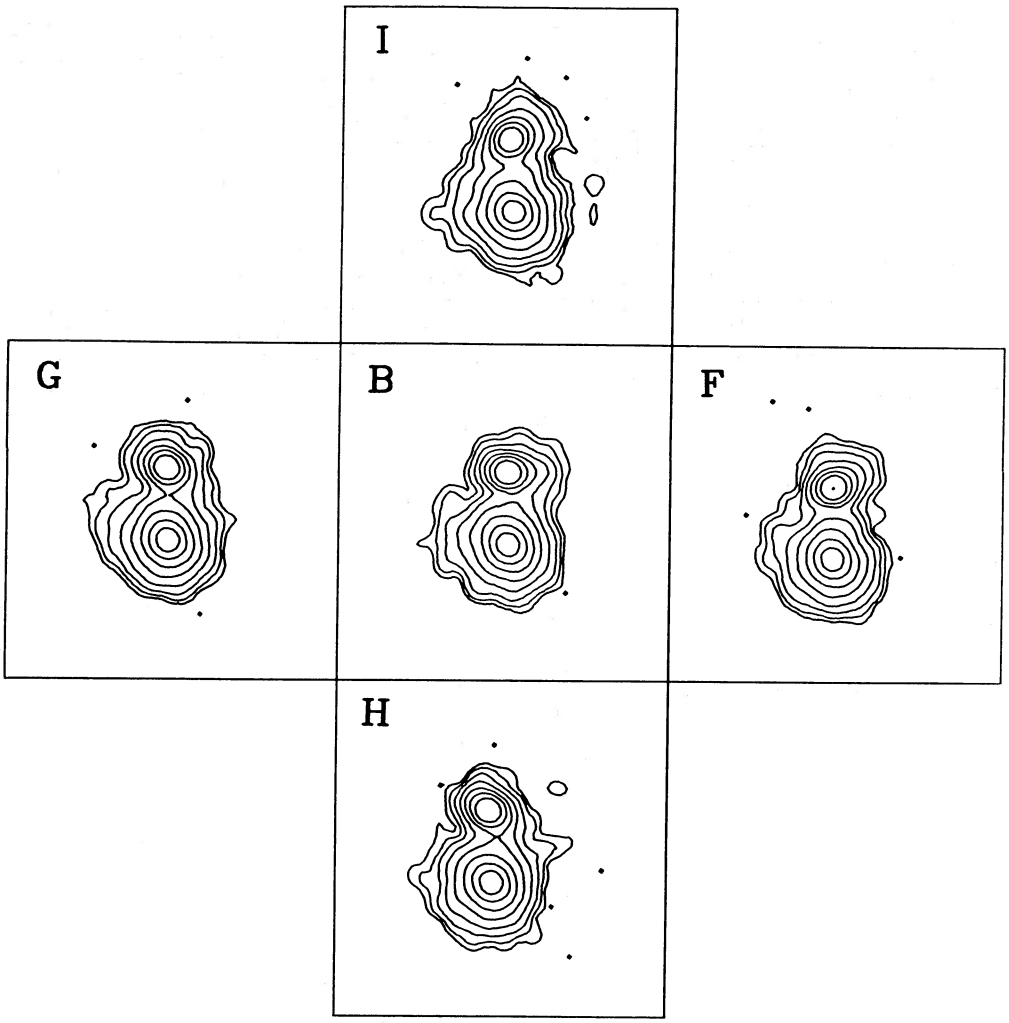

FIG. 4.—Similar to Fig. 3, except as follows. Boxes F and G show models for which the M_2 minor axis is precessed $\pm 30°$ from model B relative to the true position angle (i.e., orbital phase) of galaxy 2. Boxes I and H show models for which the M_2 minor axis is tilted 30° closer to and farther from the orbital rotation axis than in model B, respectively. Note in Table 2 that the M_2 minor axis for model B lies in the orbital plane and that this galaxy is assumed to be nonrotating. Note here the strong dependence of the appearance of galaxy 2 on its assumed minor axis direction.

accuracy, we believe) to which the total mass for the system can be determined by the model-matching procedure; unknown systematic errors in the velocity measurements could affect the accuracy of our mass estimate. Within the context of the present physical model and within the limits imposed by our observational errors, we have solved K99.

Figure 7 compares the observed velocity profiles for K99 with those measured in our best-fit model. Each real observation is marked by an "x," while the model data are traced by the solid curves (drawn at ± 1 σ from the mean line-of-sight velocity at each radius; the model slit width was equal to 0.10 model units, or two softening radii). Note that the rotation in K99-1 is not perfectly matched by the model, but that is a minor detail, curable by appropriate adjustments in the strength of rotation imposed on the model. A more physical rotation model would be in order here; the reflection mode of Paper II is not entirely reasonable, but does get the magnitude and shape of rotation profile nearly correct. The much-discussed U-shaped rotation curve of K99-2 (see § III*a* of Paper III) is evident in the model. It was also present in many of the near-miss models discussed in the previous section. We believe that this is proof of the action of tidal friction in K99: those stars in the wings of the "U" are those carrying away the binary orbital angular momentum.

In Figure 12 we present images of the real surface brightness data and of the model surface density data for K99 (and also for K564, to be discussed later). Note how the asymmetric mass distribution in galaxy 1 and the tail on galaxy 2 match those features in the observations. Note also how the position angle and degree of flattening in each of the two model galaxies match those seen in the CCD image. It is clear that the distortions observed in K99 are explainable by tidal gravitational phenomena alone. The expected motion for the components of K99 in the directions opposing their distended sides, which was discussed in Paper II, is confirmed by the model presented here, as well as in all of our test models. It can be said, with little room for doubt, that such light distributions (i.e., distortions of opposite parity in close pairs of galaxies) will be a sure indicator of the sense of binary motion in pairs that are so disturbed.

Since the galaxies in K99 are not strongly disrupted, it appears certain that their initial relative trajectory was a slight-

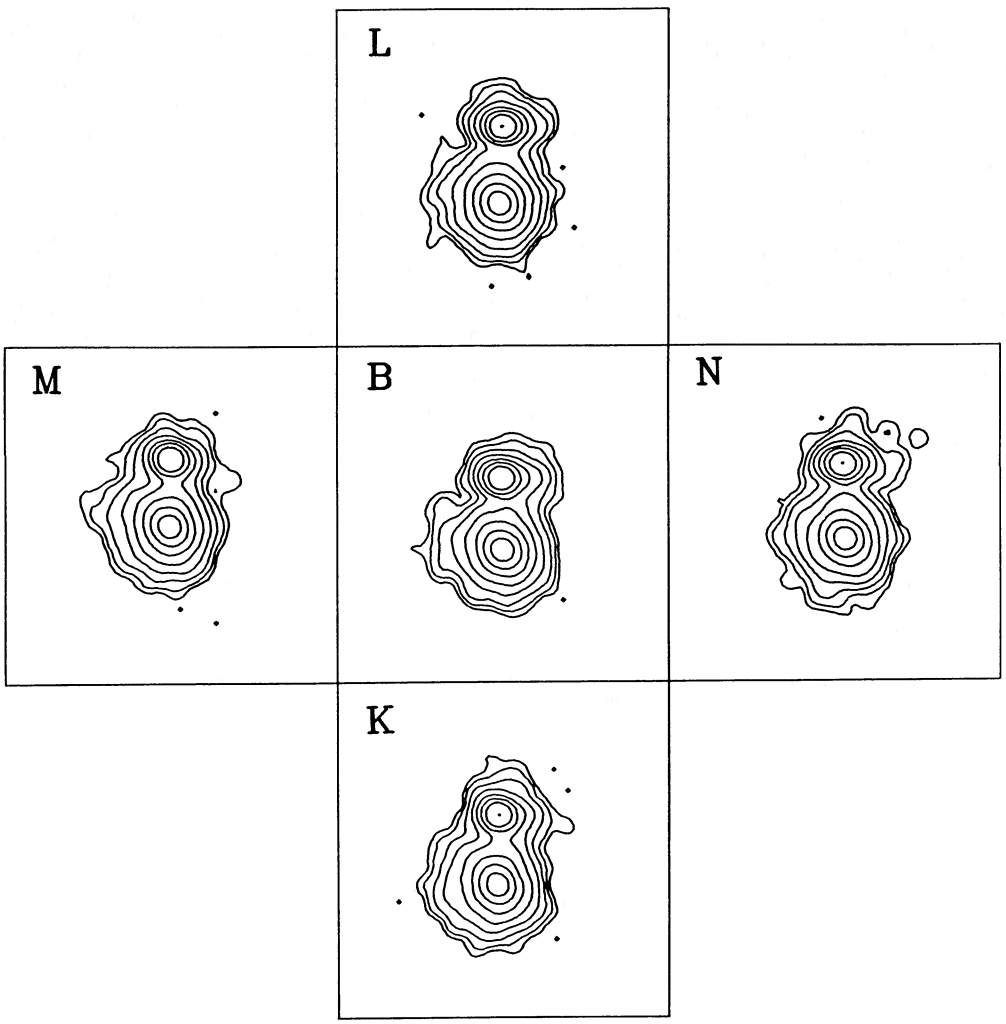

FIG. 5.—Similar to Fig. 3, except as follows. Boxes K and L show models for which the orbital pericenter separation is decreased and increased by ~10% respectively, relative to that for model B. Boxes M and N show models for which the orbital pericenter speed is decreased and increased by ~5%, respectively, relative to the average of the values found for the best models in Table 2: B and J. Note the affect of these orbital variations on the appearance and disappearance of the tidal tail(s) emanating from galaxy 2.

ly unbound one, of moderate eccentricity. Otherwise, if the orbital eccentricity of the pair was small, the galaxies would have been in close proximity for many orbital periods and their distortions would be much more severe than is observed and we should have detected an extended smooth background of starlight. On the other hand, if the orbital eccentricity was large (i.e., the pair is on a strongly unbound trajectory), there would be very little distortion in the two galaxies until they were far apart (i.e., they would now appear close only in projection). But, by then, K99-2 would no longer be able to dynamically support the actually observed nonsteady U-shaped rotation.

III. SIMULATIONS OF K564

Simulations are presented in this section representing (*a*) the best match to the observational data for K564 and (*b*) a collection of some of the failed attempts to match the data. The results from a coarse study of the orbital parameter space are presented first in Figures 8 and 9, followed in Figure 10 by a finer resolution investigation of that space and of the internal galaxy parameter space. Tables 3 and 4 list the model parameters for the various simulations that are portrayed in this series of surface density contour diagrams. Figures 11 and 12, with Table 5, present the adopted physical solution for K564: rotation and dispersion velocity profiles, a surface density contour "image," and a tabulation of the orbit properties (e.g., orbit inclination, orbital phase, line of nodes, masses, and merger time).

a) K564 Mass Ratio

The ratio of the velocity dispersions for the two components of K564 is consistent with unity (see Table 2 of Paper III). The luminosity ratio is similarly consistent with unity, as can be seen roughly from a look at Figures 6 and 7 of Paper III. Although the southeast component of K564 (hereafter K564-1) does appear to have a somewhat larger isophotal diameter, there is no compelling reason to believe that this is due to a mass difference rather than being due its tidal response being different from its companion's. A few preliminary models (not reported here) were run with mass ratios differing from unity by more than 20%; in all of these, either the tidal distortions in the galaxies could not be matched or the ratio of

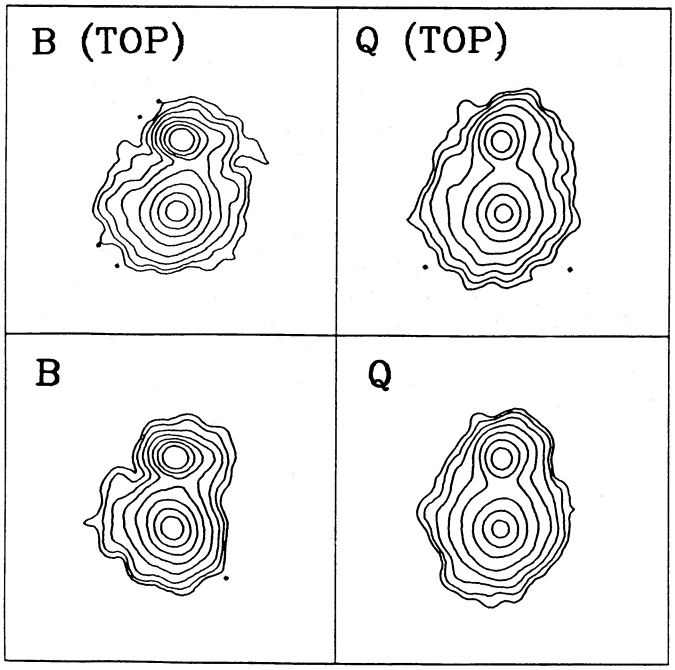

FIG. 6.—Top views (i.e., down the orbital rotation axis) and oblique views of the best-fit model B for K99 and of a model with the same orbital parameters but with different internal parameters. In particular, for model Q, (i) the rotation axis for galaxy 1 coincides with the orbital rotation axis, and (ii) neither model galaxy is flattened. Note here the nearly total absence of distortions in the model Q galaxies. Note also that this model is nearly identical to model 14 of Fig. 2. For the oblique views, the "observer" is located at an inclination 40° above the orbital plane at an azimuth 105° measured *clockwise* in the orbital plane from the position angle of galaxy 2, the smaller component.

central velocity dispersions for the two model galaxies was inconsistent with the observed ratio or both. Consequently, equal mass galaxies were used in each K564 simulation reported in this paper. For all of these simulations, except for that shown in Figure 12, the numbers of test particles comprising the two galaxies were $N_1 = N_2 = 1000$. The adopted best-fit model for K564 is portrayed in Figure 12 through a simulation in which $N_1 = N_2 = 2000$.

b) Internal Galaxy Properties

From the weak but significant rotation observed in the two galaxies comprising K564 (Fig. 9 of Paper III), it seemed fair to assume that rotation should be included in the models for K564, although not as a high priority item. What was not initially apparent was that rotation would be essential to finding a good fit to the observed distortions in the image of K564 (Fig. 7 of Paper III). The tidal coupling between the binary orbit and the internal, ordered motions of the stars comprising each rotating galaxy proved directly responsible for the observed distortions (see the extensive discussion, in the context of K99, appearing in § III*a* of Paper III). Models with no rotation did not show the strong isophotal twisting seen in the northwest component of K564 (hereafter K564-2), and those models could not reproduce the photometric distortions seen in either galaxy. It became clear after many modeling attempts that rotation was a prerequisite to a successful model search for K564.

The type of rotation included in our models also proved to be strongly restricted. A comprehensive study of orbital parameter space was carried out initially using, for both galaxy 1 and 2, the circular rotation mode that was discussed in § V*b* of Paper II. These model galaxies reacted much too strongly to

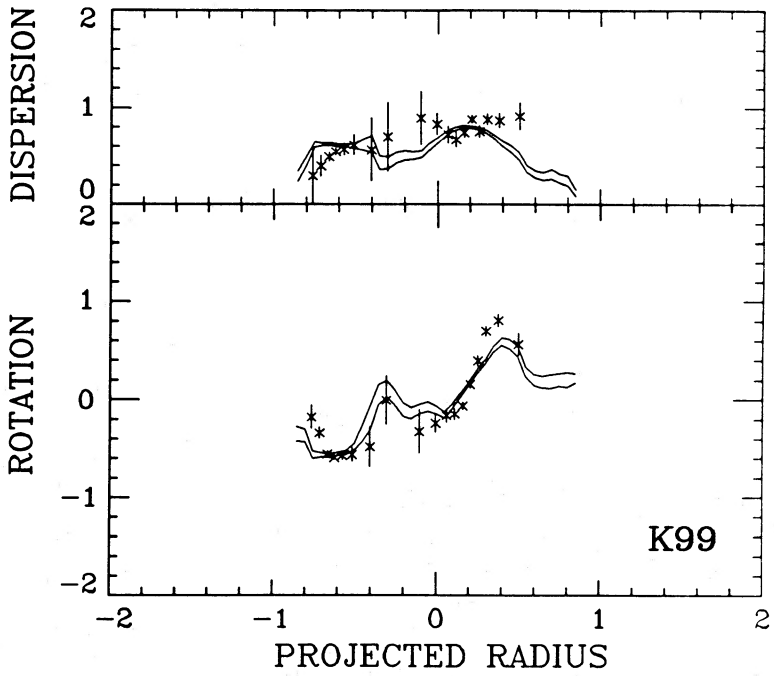

FIG. 7.—Velocity profiles for the real and modeled K99 galaxies as measured along a line connecting their centers. Each real data point is marked by an "X," to which a bar is attached indicating the relative measurement error (see Paper III). The velocity units are scaled to that of the model, where 1 unit = 260 km s^{-1}. The model velocities are represented by two curves: for each position along the slit, these lines pass through points at the mean velocity ± one standard deviation (see Paper II).

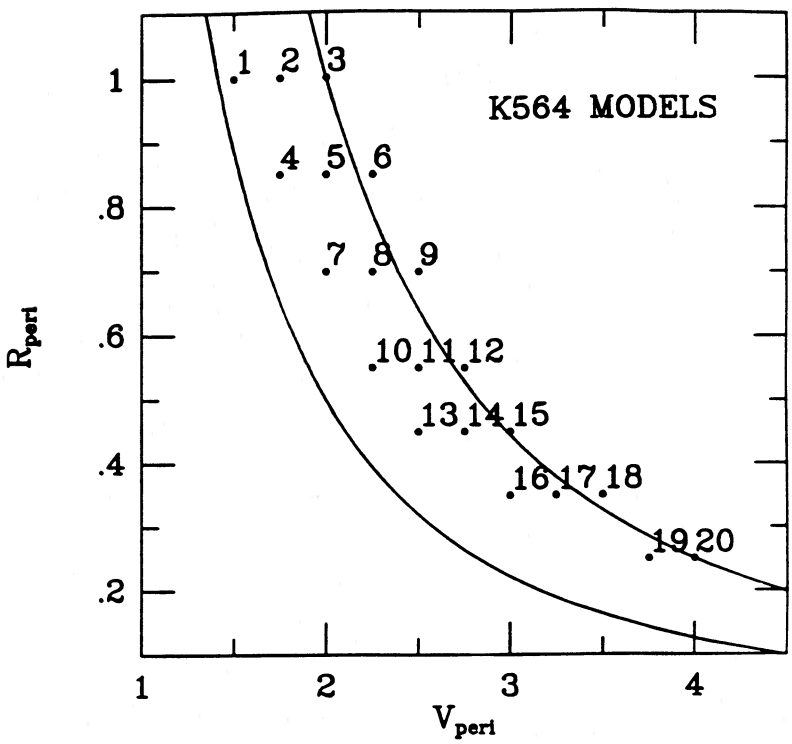

FIG. 8.—Similar to Fig. 1, except that here are plotted the positions of orbits in the orbital parameter space for the models listed in Table 3 for K564

the tidal field of their companion. Long tidal tails developed, reminiscent of the now-legend disk-disk models of Toomre and Toomre (1972). There was not a single orbit that provided even an approximate match to the K564 image. It was determined after many failed simulations that the reflction algorithm (§ Vc of Paper II) allowed for the only reasonable match to the observations of K564. In all of the models described below, the rotation of both galaxy 1 and galaxy 2 was generated with 100% particle participation in the reflection mode. For the models shown in Figure 9, the rotation axes were pointing at the observer, who was viewing down the binary angular rotation axis. Models for K564 shown in subsequent figures have the rotation axes tilted at an oblique angle relative to observer and orbital rotation axis.

For all of the model galaxies discussed in this paper it was assumed that the minor axis is coincident with the rotation axis. Since both K564-1 and K564-2 show a measurable ellipticity in Figure 7 of Paper III, this assumption alone, if not common sense, then dictates the use of a nonzero oblique angle for the inclination between observer and rotation axis. Such

TABLE 3

MODEL PARAMETERS FOR K564 ORBIT SEARCH

MODEL NUMBER	M_2/M_1	R_{peri}	V_{peri}	M_1 ROTATION			M_2 ROTATION			REMARKS
				M_1	Mode	Axis	M_2	Mode	Axis	
1.....	1	1.00	1.50	E0	Refl	(0, 0)	E0	Refl	(0, 0)	Too slow
2.....	1	1.00	1.75	E0	Refl	(0, 0)	E0	Refl	(0, 0)	Too distant
3.....	1	1.00	2.00	E0	Refl	(0, 0)	E0	Refl	(0, 0)	Too weak
4.....	1	0.85	1.75	E0	Refl	(0, 0)	E0	Refl	(0, 0)	Too slow
5.....	1	0.85	2.00	E0	Refl	(0, 0)	E0	Refl	(0, 0)	Too distant
6.....	1	0.85	2.25	E0	Refl	(0, 0)	E0	Refl	(0, 0)	Too weak
7.....	1	0.70	2.00	E0	Refl	(0, 0)	E0	Refl	(0, 0)	Studied in detail
8.....	1	0.70	2.25	E0	Refl	(0, 0)	E0	Refl	(0, 0)	Too distant
9.....	1	0.70	2.50	E0	Refl	(0, 0)	E0	Refl	(0, 0)	Too distant
10.....	1	0.55	2.25	E0	Refl	(0, 0)	E0	Refl	(0, 0)	Studied in detail
11.....	1	0.55	2.50	E0	Refl	(0, 0)	E0	Refl	(0, 0)	Poor fit to data
12.....	1	0.55	2.75	E0	Refl	(0, 0)	E0	Refl	(0, 0)	Poor fit to data
13.....	1	0.45	2.50	E0	Refl	(0, 0)	E0	Refl	(0, 0)	Studied in detail
14.....	1	0.45	2.75	E0	Refl	(0, 0)	E0	Refl	(0, 0)	Poor fit to data
15.....	1	0.45	3.00	E0	Refl	(0, 0)	E0	Refl	(0, 0)	Poor fit to data
16.....	1	0.35	3.00	E0	Refl	(0, 0)	E0	Refl	(0, 0)	Studied in detail
17.....	1	0.35	3.25	E0	Refl	(0, 0)	E0	Refl	(0, 0)	Poor fit to data
18.....	1	0.35	3.50	E0	Refl	(0, 0)	E0	Refl	(0, 0)	Poor fit to data
19.....	1	0.25	3.75	E0	Refl	(0, 0)	E0	Refl	(0, 0)	Too strong
20.....	1	0.25	4.00	E0	Refl	(0, 0)	E0	Refl	(0, 0)	Too strong

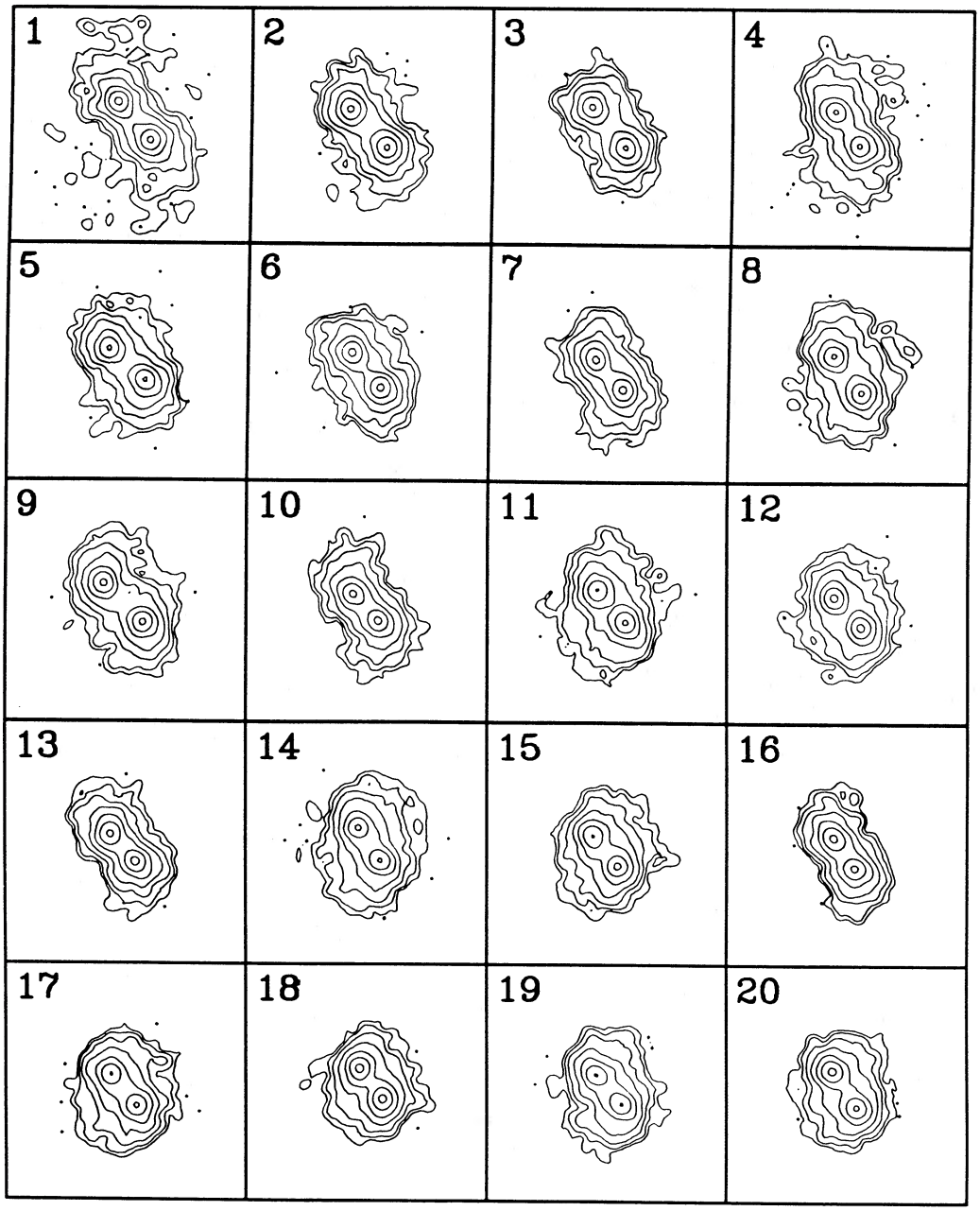

FIG. 9.—Similar to Fig. 2, except that here are presented top views of the attempted models for K564, with each box numbered according to the key in Table 3 (and Fig. 8). As in Fig. 2, each model is shown at the time when the separation of the pair and the degree of distortion are as close to the real data as the simulation allows. Note here, as before, the variations in the distortions as a function of the orbital parameters.

was already alluded to above. As was done for K99, a series of models were run here for K564 specifically to test for the effects of orbital variations on the appearance of distortions in the model galaxies. For these, flattening was not included. Results from these tests are shown in Figure 9. All subsequent figures present models in which each galaxy has nonzero flattening (compare Tables 3 and 4). The intrinsic flattening of each model galaxy was fixed to be that of an E3 galaxy, similar to what was done for K99-1, in order to test the effects of varying the most significant model parameters. Again, the important parameters were (i) the orbit parameters, $V_{\rm peri}$ and $R_{\rm peri}$, and (ii) the directions of the M_1 and M_2 rotation/minor axes (where M_1 represents K564-1 and M_2 represents K564-2).

c) *Possible Orbits for K564*

The $R_{\rm peri} - V_{\rm peri}$ diagram was used once more to help isolate a unique orbital solution for K564. Figure 8 presents the relevant diagram for unit mass ratio in our model units (see § IIc). The two curved lines again represent the locus of circular orbits (*lower curve*) and of parabolic orbits (*upper curve*). As for K99, we tested some strongly unbound orbits for K564 and again found that the resultant tidal distortions were much too small compared to observation.

We present initially the results from studying 20 possible orbits for K564. All bound-orbit simulations began with the galaxies at apocenter and all unbound models began 8–10

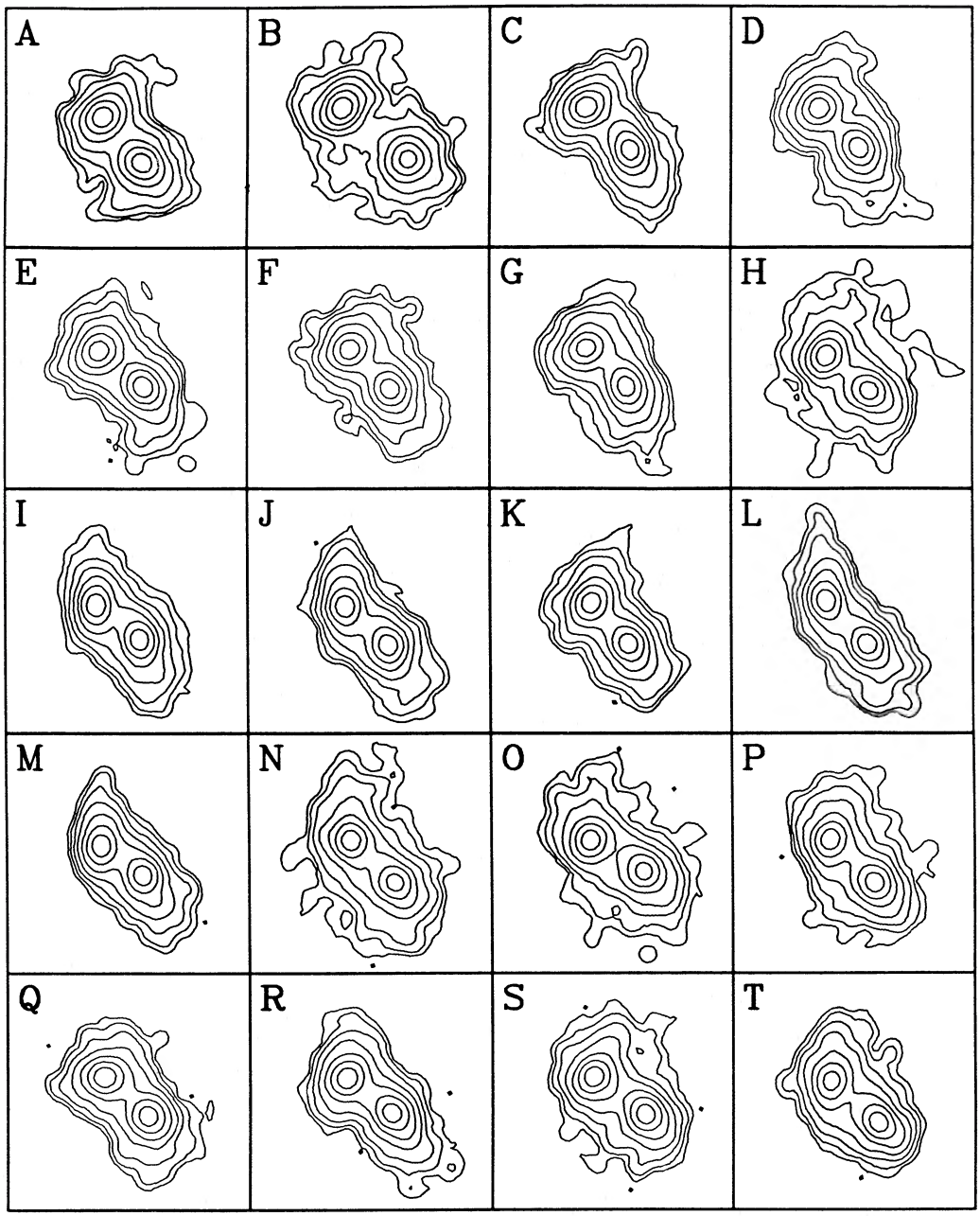

FIG. 10.—Surface density contours of flattened K564 models with orbital parameters corresponding to the apparently best-fit models of Fig. 9. As in that figure, each model is shown from the top (i.e., down the orbital rotation axis) at a time that allows the best match to the photometric data. (Observing these models from the orbital pole is almost certainly required by the tiny relative velocity, ≈ 26 km s^{-1}, observed for the pair). Each box is labeled according to the key in Table 4. Various dependences are shown in this series of simulations: the effects of orbital variations and of rotation axis variations in the two model galaxies. Note that model N represents our best-fit to the K564 pair.

crossing times prior to pericenter passage. The 20 orbits that were studied are identified in Figure 8 with labels corresponding to the model numbers given in Table 3. Figure 9 uses these same model numbers in a display of the best possible matches between the imaging data for K564 and the model binary galaxies evolved along these orbits.

Table 3 tabulates the initial parameter values for the 20 possible orbits of K564 that were identified in Figure 8. In all of these orbits, the following inputs were constant: the mass ratio ($M_2/M_1 = 1$), the number of test particles ($N_1 = N_2 = 1000$), the lack of flattening in M_1 and M_2 (both E0), and the rotation properties of M_1 and M_2. As stated earlier, both M_1 and M_2 had 100% particle participation in the reflection mode of rotation, with the axis of rotation parallel to the orbital angular momentum axis, pointing in the polar-coordinate direction $\theta = 0°$. The models listed in Table 3 differ only in their initial orbits, as specified by $R_{\rm peri}$ and $V_{\rm peri}$. As for K99, the lower numbered orbits represent slow encounters, while the higher numbered orbits are fast. The leftmost points in each line of models shown in Figure 8 are those with the strongest tidal impulse (see discussion for K99); those on the right are weakest. Table 3 includes remarks on the outcome of the

TABLE 4

MODEL PARAMETERS USED TO FIND UNIQUE SOLUTION FOR K564

MODEL	R_{peri}	V_{peri}	M_1	ROTATION Mode	ROTATION Axis	M_2	ROTATION Mode	ROTATION Axis	AREAS OF MISMATCH IN SURFACE DENSITY MAPS
A	0.70	2.00	E3	Refl	(60, 75)	E3	Refl	(75, 0)	P.A. of distortions
B	0.70	2.25	E3	Refl	(150, 80)	E3	Refl	(75, 170)	Distortions/flattening
C	0.55	2.15	E3	Refl	(60, 75)	E3	Refl	(75, 165)	P.A. of distortions
D	0.55	2.25	E3	Refl	(60, 80)	E3	Refl	(75, 170)	P.A. of M_2 distortion
E	0.55	2.25	E3	Refl	(60, −100)	E3	Refl	(75, −10)	Shape of M_2 distortion
F	0.55	2.25	E3	Refl	(60, 90)	E3	Refl	(75, 170)	Shape of distortions
G	0.55	2.25	E3	Refl	(60, 70)	E3	Refl	(75, 160)	Shape of M_2 distortion
H	0.55	2.35	E3	Refl	(60, 95)	E3	Refl	(75, 185)	Relative tides
I	0.45	2.50	E3	Refl	(60, 55)	E3	Refl	(75, 35)	Details of distortions
J	0.45	2.50	E3	Refl	(60, 75)	E3	Refl	(75, 35)	Details of distortions
K	0.45	2.50	E3	Refl	(60, 90)	E3	Refl	(75, 5)	P.A. of distortions
L	0.45	2.50	E3	Refl	(60, 90)	E3	Refl	(75, 55)	Shape of M_2 distortion
M	0.45	2.40	E3	Refl	(60, 70)	E3	Refl	(75, 30)	Details of distortions
N	0.45	2.60	E3	Refl	(60, 85)	E3	Refl	(75, 40)	None
O	0.45	2.70	E3	Refl	(60, 60)	E3	Refl	(75, 20)	Weak distortion in M_1
P	0.45	2.80	E3	Refl	(60, 80)	E3	Refl	(75, 30)	Weak distortion in M_1
Q	0.35	3.00	E3	Refl	(45, −100)	E3	Refl	(75, −20)	Shape of M_2 distortion
R	0.35	3.00	E3	Refl	(60, 85)	E3	Refl	(75, 10)	Shape of M_2 distortion
S	0.35	3.25	E3	Refl	(60, −100)	E3	Refl	(75, 5)	Weak distortion in M_1
T	0.35	3.25	E3	Refl	(60, 80)	E3	Refl	(75, 25)	Weak distortion in M_1

various simulations, which are portrayed in Figure 9, where the numbered boxes correspond to the model numbers in Table 3 (and Fig. 8). The time of observation for each of these models was chosen to be that which offered the best possible match to the observed distortions in K564. Note the correlation between the observed tidal distortion in the galaxies and the remarks offered in Table 3.

Several orbits in Table 3 resulted in strong candidates for possible models of K564. Compare Figure 7 of Paper III with models 7, 10, 13, and 16 of Figure 9 and note that these orbits have similar tidal impulse. Because of our nearly pole-on view of K564 (i.e., very small relative velocity), it was not possible to reject any of these four models on the basis of velocity data alone. This was unlike our experience with K99, where the look-alike models were removed from consideration when their velocities could not match those observed (see the discussion at the end of § IIc). For K564, we were forced to study each of the four models listed above in great detail with realistic rotation axes and flattenings for the two galaxies. It was only after a tedious, methodical, and painstaking investigation of the full parameter space available to our models that we finally and unequivocally found the unique solution to K564. That investigation is outlined below, where the importance of using the internal galaxy parameters becomes apparent.

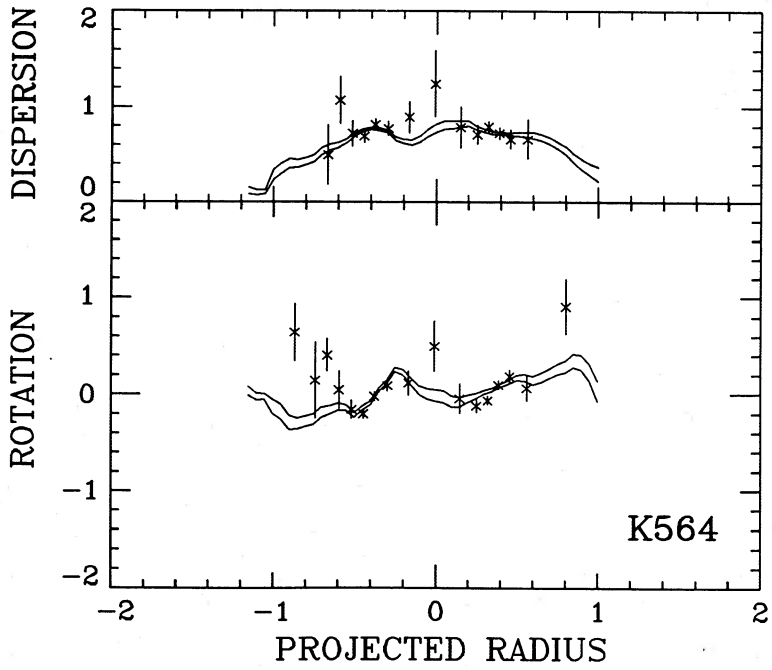

FIG. 11.—Same as Fig. 7 except that these are the velocity profiles for the real and modeled K564 galaxies. Here one velocity unit = 240 km s^{-1}.

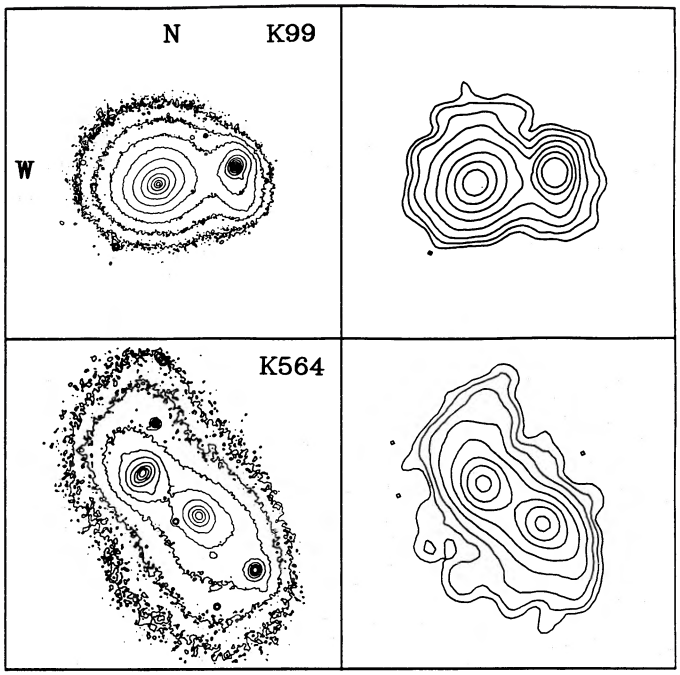

FIG. 12.—Reproductions of (i) the photometric observations reported in Paper III for K99 and K564 and (ii) the best-fit models for K99 (model B of Table 2) and for K564 (model N of Table 4). (As in Paper III, east is to the right and west to the left in these depictions of the CCD images, reversed from the sky.) Note the agreement in detail between model and observation. Although the strong flattening in the central regions of the northwest component of K564 is not evident in its model, the correct ellipticity is in fact included in the model at the correct position angle; this flattening becomes unobservable in the simulation after a period of time due to the assumed sphericity of our model potential (see Paper II). These K99 and K564 models were run with 4000 test particles, apportioned in each case according to the assumed binary mass ratio. For K99, this is the same model B that appears in Figs. 3–6, for which $N_1 = 3000$ and $N_2 = 1000$. For K564, the simulation shown here differs from model N of Fig. 10 only in the total number of particles employed: in that simulation (as in all other attempts to model K564) $N_1 = N_2 = 1000$, whereas the simulation shown here has $N_1 = N_2 = 2000$.

TABLE 5

ADOPTED PHYSICAL PARAMETERS

Parameter	K99	K564
Mass-weighted redshift ($\Delta\lambda/\lambda$) for binary	0.01206 ± 0.00003	0.02725 ± 0.00003
Distance (Mpc h^{-1})	36.1	81.7
Projected relative velocity (km s^{-1})	198 ± 13	26 ± 16
Projected separation (kpc h^{-1})	10.2 ± 0.2[a]	13.1 ± 0.4[a]
Mass ratio (M_2/M_1)	1/3	1
Orbital eccentricity	1.25 ± 0.2[b]	0.5 ± 0.1[b]
Orbit inclination	$50° \pm 2°$[b]	$7°.2 \pm 0°.2$[c]
P.A. of line of nodes (from north)	$70° \pm 10°$[b]	$115° \pm 10°$[c]
Orbital phase (from line of nodes)	$15° \pm 10°$[b]	$10° \pm 10°$[c]
Mass projection factor[d]	2.8 ± 0.4[b]	230 ± 30[b]
Total mass ($10^{11} M_\odot\ h^{-1}$)	2.6 ± 0.4[b]	4.7 ± 0.6[b]
Total absolute B magnitude[e]	-20.33	-21.19
M_T/L_B ($hM_\odot/L_\odot$)	12 ± 2[b]	10 ± 2[b]
M_1 ($10^{11} M_\odot\ h^{-1}$)	1.95 ± 0.4[b]	2.4 ± 0.4[b]
Virial estimate for M_1 ($10^{11} M_\odot\ h^{-1}$)	2.3[f]	5.5
M_2 ($10^{11} M_\odot\ h^{-1}$)	0.65 ± 0.1[b]	2.4 ± 0.4[b]
Virial estimate for M_2 ($10^{11} M_\odot\ h^{-1}$)	0.5	6.2
Time until merger	∞ (remains unbound)	5×10^8 yr

[a] Uncertainty in locating galaxy center on CCD image.

[b] These estimates are derived from the best matching simulation for each pair. The given uncertainties represent the full range of allowable parameter values.

[c] The inclination angles and orbital phase for K564 are strongly correlated due to the nearly pole-on viewing angle: small variations in inclination are allowed without significantly affecting the appearance of the projected mass distribution. However, in doing that, the match to the observed velocities is preserved by forcing the observer to another azimuthal angle relative to the binary separation vector. One of those sets of allowed angles is given here. For a given inclination, the quoted uncertainties represent the range of angles that allow the model to match the observed velocities.

[d] Projection factor k is estimated for the best matching simulations from: $k = G(M_1 + M_2)(\Delta v_{\rm proj})^{-2} S_{\rm proj}^{-1}$.

[e] Luminosity determined from recent photometric imaging data to be presented in a later paper. Calculated with $h = 1$ and $q_0 = \frac{1}{2}$. Includes the galactic reddening correction from Burstein and Heiles 1982. The absolute photometry is accurate to 0.06B mag.

[f] From the rotation curve, we estimate $M_1 \approx 0.1 \times 10^{11}\ M_\odot$, if the mass is entirely rotation supported (excludes an unknown correction for the inclination of the rotation axis).

d) Isolating a Unique Model for K564

In this section we present a series of simulations around the four different models that were described in the previous section as being apparent solutions for K564. These are presented in order to demonstrate that only one of those four can in fact match all of the detailed observations of the system. The degree to which the unique solution can be isolated in parameter space is also given some attention, although the results of that extensive investigation are presented not nearly so systematically as was done for K99 in § II*d*.

Table 4 tabulates the range of model parameters used to locate the unique solution for K564. Twenty models are listed, each assigned a letter designation corresponding to a surface density map in Figure 10. Among the 20 models, the following inputs were constant: the mass ratio ($M_2/M_1 = 1$), the number of test particles ($N_1 = 1000$ and $N_2 = 1000$), the ellipticity of the two galaxies (E3), and the rotation modes of the two galaxies (100% particle participation in the reflection mode). Between the 20 models, the differences were the orbit parameters ($R_{\rm peri}$ and $V_{\rm peri}$), the direction of the M_1 rotation/minor axis, and the direction of the M_2 rotation/minor axis. Brief remarks are recorded in Table 4 indicating why a particular model failed to match the imaging data for K564. In most cases, the failure is obvious; in others, the mismatch is more in the fine details of the surface density map: the extent of the tidal lobes and/or the position angle of the lobes. All of the models depicted in Figure 10 are shown at the time when its appearance most nearly matched the observations of K564.

Models A and B of Table 4 (and Fig. 10) test the validity of model 7 from Table 3 (and Fig. 9). These fail because bound, large $R_{\rm peri}$ trajectories lead to distortions in the galaxies that are nearly always orthogonal to the line connecting the galaxy centers. This is clearly unacceptable. No manipulation of the minor axis directions made up for this deficiency without also destroying the observed flattening orientations of the galaxies relative to the line of centers. Model B shows how round the isophotes of galaxy 1 appear when its minor axis is pointing just 30° closer to the direction of the observer.

Models C–H of Table 4 (and Fig. 10) test the validity of model 10 from Table 3 (and Fig. 9). These failed essentially for the same reasons as models A and B failed (see above). Models D–G specifically demonstrate the uselessness of trying to adjust the minor axis directions.

Models I–P of Table 4 (and Fig. 10) test the validity of model 13 from Table 3 (and Fig. 9). In particular, models I–L test the effects of varying the internal galaxy parameters, while models M–P examine the consequences of moving around in the orbital parameter space (Fig. 8). Model I looks too much like two flattened galaxies projected side-by-side; there is no real evidence of isophote twisting. Models, J, K, and L all have the distension on galaxy 1 at a position angle too close to that of the line of centers. Models K and L show the effects of trying to adjust the minor axis of galaxy 2. Model M corresponds to a strong-tide orbit that makes the distortions on galaxy 2 too large. Model N is the one we have been looking for: our best-fit model. Models O and P are weak-tide orbits; there is not enough time before the galaxies separate for significant distortions to build up in galaxy 1, even though galaxy 2 is not too far wrong. Model N, again, is one that we believe offers the best match to the available observational data on K564. It matches in (i) the strength of the tides, (ii) the position angle of the tidal lobes, (iii) the asymmetry of the tidal distortions, (iv) the flattenings and position angles in the central regions of the galaxies (even though this is hard to see here, see discussion of Fig. 12 below), and (v) its velocity profiles (Fig. 11, discussed below).

Models Q–T of Table 4 (and Fig. 10) test the validity of model 16 from Table 3 (and Fig. 9). These fail either because the encounter is too fast for much distortion to develop (as in Models S and T), or because small $R_{\rm peri}$ trajectories lead to distortions in the galaxies that are more along the line of centers than at the required oblique angle (see models Q and R). Adjusting the minor axis directions do not solve the problem, as shown in model Q where galaxy 2 shows both leading and trailing distensions. It is very hard with these orbits to have galaxy 2 flattened in accordance with the inner isophotes of Figure 7 in Paper II and, from that, to get a one-sided tidal distortion also. Model Q shows how round the isophotes in galaxy 1 become when its minor axis is pointing a mere 15° closer to the direction of the observer than in the other simulations that are displayed.

e) The Adopted K564 Solution

Model N of Table 4 provides the input model parameters for the simulation that best matches all of the observations for K564. In Table 5 the derived physical properties and projection angles for K564 are tabulated, including a value for the absolute B magnitude that was obtained from the photometric study mentioned in § II*e*. Note the precision to which the total mass for the system can be determined by the model-matching procedure. Even though systematic errors in the velocity measurements could affect the accuracy of our mass estimate, one should not be concerned about the large percentage error in our measured relative velocity (26 ± 16 km s^{-1}) since the mass scale is set almost entirely by the observed velocity dispersions, and our dispersion measurements are quite reasonable.

The virial mass estimates in Table 5 differ by factors up to 2.5 from the mass estimates derived from our simulations. For three of the four galaxies, our values are lower. This is consistent with the remarks by Tonry (1983), who summarized the conclusions of several authors when he said that the Poveda (1958) formula for virial masses actually overestimates the true mass of a galaxy by factors as large as 2. We are greatly encouraged by this, and we believe that, within the context of the present physical model and within the limits imposed by our observational errors, we have correctly determined the projection factors and masses for the K99 and K564 pairs.

Figure 11 compares the velocity profiles observed in K564 with those measured in our best-fit model. Each real observation is marked by an "x," while the model data are traced by the solid curves (see description of Fig. 7 in § II*e*). The dispersion profile is nearly a perfect match, while the rotation profile is correct in form if not in point-by-point detail.

In Figure 12 we present contour maps of the K564 surface brightness data and of the model surface density data. Note how the asymmetric mass distributions in each model galaxy match the photometric distortions seen in the real observations. The fit is especially good at reproducing the magnitude and position angles of the asymmetries seen at large radii. However, the degree of flattening at small radii does not provide an excellent match to that seen in the CCD image. This is not considered to be a problem; K564-2 (the northwest component) actually was modeled with a galaxy having the correct flattening at the proper orientation. Those details should have been visible in the model, but they were washed out over time as the galaxy responded to the spherical poten-

tial imposed on our model (see Papers I and II) and as the small number of particles in the simulated galaxy departed from their flattening restriction while responding to the strong tidal field of the companion galaxy. Hence, the apparent discrepancy between model and observation at small radii is an artifact both of our choice of a model potential and of small-numbers statistics; it is not a true mismatch.

As was the case for K99, the distortions observed in K564 can be entirely explained by the action of tidal gravity, with the components of the galaxy pair moving in the direction that one would intuitively guess: in the direction toward which their surface brightness contours are crowding upon one another. The distended sides of the K564 galaxies are trailing behind the bulk motion of their attached galaxies.

Since the galaxies in K564 are strongly disturbed, it appears certain that their relative trajectory is a bound one, of moderate (not small) eccentricity. Applying the same arguments that were used for K99: if the orbital eccentricity of the pair was small, the galaxies would have been in close proximity for many orbital periods and their distortions would be much more severe than is observed and there should have been evidence for an extended smooth background of starlight. On the other hand, if the orbital eccentricity was large (i.e., the pair is on an unbound trajectory), there would not be such a large distortion in each of these very close galaxies when they are viewed from the pole (where the projected separation nearly equals the true separation). It therefore seems likely that we are viewing a recently captured binary and that the line of sight to K564 cannot be far from the axis of binary revolution since the observed velocity difference is so small.

IV. SUMMARY AND CONCLUDING REMARKS

It has been demonstrated that both the velocities and the distorted light distributions for at least two pairs of elliptical galaxies are completely reproducible by a simple gravitational model. This confirms the validity of Newtonian gravity on scales up to the size of these binary systems (10–20 kpc). Because gravity is scale-free, unlike the gasdynamical processes active in spiral galaxies, the physical model employed here will apply to any pair of colliding ellipticals, whether supergiants or dwarfs. It has also been shown that it is possible to constrain the physical parameters that describe the binary. This is accomplished specifically through the application of positional spectroscopic data, such as that obtained with the HGVS at KPNO (Paper III). Surface photometric observations are of great value when the faintest parts of the galaxies are detected; those outer parts are most sensitive to tidal gravitational fields and are thus a good probe of such forces. Yet imaging data alone are insufficient to identify uniquely the correct model for a particular system. Spectroscopic measurements are essential to isolating the unique solution. As with the imaging data, the further from the center of a disturbed galaxy that one measures velocities, the greater will be our understanding of the properties of colliding galaxies and the greater will be our opportunity to probe the large-scale mass distribution in galaxies. This has been emphasized by Rots (1978), Combes *et al.* (1980), and van der Hulst (1978, 1979); all of these have presented dynamical models of particular interacting galaxy systems and have made a case for the use of wide-field velocity measurements. Jenkins (1981) has likewise demonstrated the value of long-slit spectroscopy; he argues that the peculiar velocity fields observed in several radio ellipticals are evidence of a merger origin for these galaxies. Many viable simulations can be found that match only the images of tidally disturbed galaxy pairs; it is the long-slit velocity data that truly constrain the projection factors, mass estimates, and internal dynamics. However, as mentioned in Paper III, much can still be learned if only central redshifts, central dispersions, and good surface photometry were available. It is argued in Paper II that the ratios $S_{\rm proj}/R_{\rm eff}$and $\Delta v/\sigma_0$ play the major role in solving for the spatial projection factors of a pair (where $S_{\rm proj}$ is the projected binary separation, $R_{\rm eff}$ is the effective radius for one of the galaxies, Δv is the line-of-sight relative velocity of the pair, and σ_0 is the central velocity dispersion for one of the galaxies). Although such a limited data set provides little insight into the internal dynamical properties of the individual galaxies in a pair, we could still use those measurements to derive the galaxy masses and the binary orbital configuration (as in Paper V).

Of further observational and theoretical interest is the possible usefulness of these simulations in distinguishing prolate from oblate galaxies. The development of a prolate galaxy from an initially axisymmetric state is one of the possible natural outcomes of a tidal encounter if the pericenter separation is small enough. Although such an approach was not taken here, it would be possible to begin a simulation with a prolate galaxy model, let the interaction proceed, and then see if the appearance of the resulting distorted galaxy is consistent with either of the galaxies in K99 or K564, or with any other interacting galaxy. If a good case can be found, then detailed spectroscopic observations would be in order.

Pairs of galaxies on strongly bound orbits or on slow, small-pericenter distance trajectories tend to experience large distortions following their point of closest approach (Fig. 2; see also Paper II, and references therein). Since very few pairs (less than 10% of the Karachentsev E-E's) are nearly so disrupted as that, it is likely that strongly bound and small $R_{\rm peri}$ orbits are underpopulated at the present epoch. Of course very few pairs will be seen near pericenter regardless of the eccentricity distribution owing to the transience of that particular configuration. But, if one of these pairs has had more than one close approach, the stars on the tidally sensitive trajectories within their parent galaxy will have been moved to some distance, if not stripped, from that galaxy in a previous pericenter passage. On subsequent approaches, the tidal splash of stars would not be nearly as impressive, and the pair of galaxies would now be seen embedded in a smooth background sea of stars. Such a distribution of light ought to be detectable and distinguishable from the luminosity distribution in a pair whose relative orbit has been slowly decaying for many orbital periods (compare Figs. 5 and 6 of Paper II). From the appearances of K99 and K564, it seems likely that these two binaries are on trajectories of moderate eccentricity (i.e., not tightly bound, nor strongly unbound). That is, these two systems possess well-defined bulges and tails, not extensive background light distributions, nor intense splashes of starlight. Studying the luminosity distribution in many more pairs will aid in the determination of the global distribution of orbital eccentricities for binary galaxies. From this distribution we could get a handle on (i) galaxy clustering on scales roughly up to 100 kpc, (ii) the expected magnitude of galaxy peculiar velocities on these scales, (iii) the frequency of close encounters, and (iv) the empirical merger rate of galaxy pairs in the universe. This last item is ripe for serious reevaluation; the most recent empirical estimate of the merger rate is the crude 10 yr old calculation reported by Toomre (1977).

To recapitulate the major results of this paper and of Papers

II and III: (1) we have developed and executed a very efficient and comprehensive simulation algorithm for the study of interacting ellipticals (Paper II); (2) we have made direct imaging observations and long-slit velocity measurements of two pairs of interacting binary galaxies, K99 and K564 (Paper III); (3) we have uncovered a strongly rotating elliptical (i.e., NGC 1587) that may already have undergone an earlier collision/merger episode (Paper III); (4) *we have detected signatures of tidal friction in action*, confirming the merger hypothesis for the evolution of colliding galaxies (this paper and Paper III; see below); (5) we have used the numerical simulation algorithm to match all of the observed data for K99 and K564, thereby validating simple Newtonian gravity on the 10 kpc scale (this paper); (6) we have uniquely determined the dynamical (orbital) status of both K99 and K564 (this paper); and (7) *we have tightly constrained the masses and spatial orientations for K99 and K564* (this paper).

Because the tidal friction hypothesis rests on simple gravitational physics, as do the simulations presented in this paper, and because we see peculiar features in our models that coincide with similar features in the observations of real interacting galaxies, we therefore expect the outcome of a close encounter between two real galaxies to coincide with the outcome of the simulations. The outcome that we expect is for bound pairs of interacting galaxies to coalesce on a time scale about equal to twice their binary orbital period (Paper I). Our descendants 50 million generations from now will know for sure the outcome of such a prediction.

I wish to thank J. Gunn, J. Hoessel, R. Kirshner, D. Richstone, and F. Schweizer for advice and encouragement and an anonymous referee for helpful suggestions.

REFERENCES

Borne, K. D. 1984, *Ap. J.*, **287**, 503 (Paper I).
———. 1988, *Ap. J.*, **330**, 38 (Paper II).
Borne, K. D., Balcells, M., and Hoessel, J. G. 1988, *Ap. J.*, submitted (Paper V).
Borne, K. D., and Hoessel, J. G. 1988, *Ap. J.*, **330**, 51 (Paper III).
Burstein, D., and Heiles, C. 1982, *A.J.*, **87**, 1165.
Combes, F., Foy, F. C., Gottesman, S. T., and Weliachew, L. 1980, *Astr. Ap.*, **84**, 85.
Faber, S. M., and Jackson, R. E. 1976, *Ap. J.*, **204**, 668.
Jenkins, C. R. 1981, *M.N.R.A.S.*, **196**, 987.
Karachentsev, I. D. 1972, *Comm. Spec. Ap. Obs. USSR.*, **7**, 3.
Poveda, A. 1958, *Bol. Obs. Tonantzintla y Tacubaya*, **17**, 3.
Rots, A. H. 1978, *A.J.*, **83**, 219.
Sargent, W. L. W., Schechter, P. L., Boksenberg, A., and Shortridge, K. 1977, *Ap. J.*, **212**, 326.
Terlevich, R., Davies, R. L., Faber, S. M., and Burstein, D. 1981, *M.N.R.A.S.*, **196**, 381.
Tonry, J. L. 1983, *Ap. J.*, **266**, 58.
Toomre, A. 1977, in *The Evolution of Galaxies and Stellar Populations*, ed. B. M. Tinsley and R. B. Larson (New Haven: Yale University Observatory), p. 401.
Toomre, A., and Toomre, J. 1972, *Ap. J.*, **178**, 623.
van der Hulst, J. M. 1978, in *IAU Symposium 77, Structure and Properties of Nearby Galaxies*, ed. E. M. Berkhuijsen and R. Wielebinski (Dordrecht: Reidel), p. 269.
———. 1979, *Astr. Ap.*, **71**, 131.

KIRK D. BORNE: Space Telescope Science Institute, Homewood Campus, Baltimore, MD 21218